

Article

Highly Active Transition Metal-Promoted CuCeMgAlO Mixed Oxide Catalysts Obtained from Multicationic LDH Precursors for the Total Oxidation of Methane

Hussein Mahdi S. Al-Aani ¹, Mihaela M. Trandafir ², Ioana Fechete ³, Lucia N. Leonat ²,
Mihaela Badea ⁴, Cătălin Negrilă ², Ionel Popescu ⁵, Mihaela Florea ² and Ioan-Cezar Marcu ^{1,5,*} 

¹ Laboratory of Chemical Technology and Catalysis, Department of Organic Chemistry, Biochemistry and Catalysis, Faculty of Chemistry, University of Bucharest, 4-12, Blv. Regina Elisabeta, 030018 Bucharest, Romania; husseinmahdi142@yahoo.com

² National Institute of Materials Physics, 405A Atomistilor Street, 077125 Magurele, Romania; mihaela.trandafir@infim.ro (M.M.T.); lucia.leonat@infim.ro (L.N.L.); catalin.negrila@infim.ro (C.N.); mihaela.florea@infim.ro (M.F.)

³ International Center for CVD Innovation-Nogent, Pôle Technologique Sud Champagne, Université de Troyes-Antenne de Nogent, 26, rue Lavoisier, 52800 Nogent, France; ioana.fechete@utt.fr

⁴ Department of Inorganic Chemistry, Faculty of Chemistry, University of Bucharest, 90-92 Panduri Str., 050663 Bucharest, Romania; e_m_badea@yahoo.com

⁵ Research Center for Catalysts and Catalytic Processes, Faculty of Chemistry, University of Bucharest, 4-12 Blv Regina Elisabeta, 030018 Bucharest, Romania; ipopescu_unibuc@yahoo.com

* Correspondence: ioancezar.marcu@chimie.unibuc.ro; Tel.: +40-21-3051464

Received: 30 April 2020; Accepted: 29 May 2020; Published: 1 June 2020



Abstract: To improve the catalytic performance of an active layered double hydroxide (LDH)-derived CuCeMgAlO mixed oxide catalyst in the total oxidation of methane, it was promoted with different transition-metal cations. Thus, two series of multicationic mixed oxides were prepared by the thermal decomposition at 750 °C of their corresponding LDH precursors synthesized by coprecipitation at constant pH of 10 under ambient atmosphere. The first series of catalysts consisted of four M(3)CuCeMgAlO mixed oxides containing 3 at.% M (M = Mn, Fe, Co, Ni), 15 at.% Cu, 10 at.% Ce (at.% with respect to cations), and with Mg/Al atomic ratio fixed to 3. The second series consisted of four Co(x)CuCeMgAlO mixed oxides with $x = 1, 3, 6,$ and 9 at.% Co, while keeping constant the Cu and Ce contents and the Mg/Al atomic ratio. All the mixed oxides were characterized by powder X-ray diffraction (XRD), transmission electron microscopy (TEM), scanning electron microscopy (SEM) coupled with X-ray energy dispersion analysis (EDX), X-ray photoelectron spectroscopy (XPS), nitrogen adsorption-desorption at -196 °C, temperature-programmed reduction under hydrogen (H_2 -TPR), and diffuse reflectance UV-VIS spectroscopy (DR UV-VIS), while thermogravimetric and differential thermal analyses (TG-DTG-DTA) together with XRD were used for the LDH precursors. The catalysts were evaluated in the total oxidation of methane, a test reaction for volatile organic compounds (VOC) abatement. Their catalytic performance was explained in correlation with their physicochemical properties and was compared with that of a reference Pd/Al₂O₃ catalyst. Among the mixed oxides studied, Co(3)CuCeMgAlO was found to be the most active catalyst, with a temperature corresponding to 50% methane conversion (T_{50}) of 438 °C, which was only 19 °C higher than that of a reference Pd/Al₂O₃ catalyst. On the other hand, this T_{50} value was ca. 25 °C lower than that observed for the unpromoted CuCeMgAlO system, accounting for the improved performance of the Co-promoted catalyst, which also showed a good stability on stream.

Keywords: layered double hydroxides; mixed oxides catalysts; transition metal; cobalt; copper; cerium; methane combustion

1. Introduction

Volatile organic compounds (VOC) are known as major contributors to air pollution, directly affecting the health of human beings through their toxic nature [1]. Moreover, these compounds contribute to the depletion of beneficial stratospheric ozone, the formation of harmful tropospheric ozone, and to the increasing of photochemical smog [1,2]. Transportation and industrial production, including the chemical and petrochemical industries, have the main contribution to the VOC emissions [1]. Depending on the sources and processes from which they come, these compounds can be alkanes, olefins, aromatics, alcohols, ketones, aldehydes, and halogenated hydrocarbons [2].

There are two kinds of methods used for the elimination of VOC: (1) Recovery methods, including condensation, absorption, adsorption, and membrane separation, and (2) destructive methods, including biofiltration, thermal oxidation, and catalytic oxidation, the destructive methods being usually more effective [1].

The most effective method for VOC destruction is their catalytic combustion, which has become commonly used for the elimination of low concentrations of VOC in the gas stream [1]. Three-fourths of the catalysts used for this process are precious metals, which are more active than metal oxides [3], but they have some disadvantages such as volatility and sintering at high temperatures, sensitivity to poisoning with sulfur compounds and water vapor, and high price [2]. On the other hand, metal oxides catalysts have specific advantages, being cheaper and easy to prepare, and having higher thermal stability and resistance to poisoning [2–4]. In the last decade, much effort has been made to find new highly active oxide-based catalytic materials with the aim of replacing the noble metal catalysts for VOC destruction, the main findings being the object of several review papers and book chapters [1,5–8].

Promising mixed oxide-based catalysts for VOC combustion were shown to be those obtained by thermal decomposition of transition metal-containing layered double hydroxides (LDH) precursors [7]. The LDH, or hydrotalcite-like compounds, are layered materials with the general formula $[M^{2+}_{1-x}M^{3+}_x(OH)_2]^{x+}(A^{n-})_{x/n} \cdot mH_2O$, with $2 \leq (1-x)/x \leq 4$, where M^{2+} and M^{3+} represent divalent and trivalent metal cations, respectively, homogeneously distributed and intimately mixed together in the hydroxide layers, A^{n-} stands for interlayered anions (inorganic or organic), and m represents the amount of water [9]. Different combinations of two or more M^{2+} and M^{3+} metal cations, including transition metals, in the brucite-like layers can lead to homogeneous mixed oxides having relatively high surface areas and good thermal stabilities, which were shown to be highly active in the total oxidation of VOC, including methane [7].

Methane is an important air pollutant, occupying the second place after carbon dioxide among the anthropogenic greenhouse gases (GHG) emitted at the global scale [10]. Also, due to its high chemical inertness, the catalytic combustion of methane is used as a model reaction to find new effective catalysts for VOC abatement. Among the LDH-derived mixed oxides, the Cu-containing systems were found to have high activity and good stability [11], their activity being a function of the copper content [12,13], the preparation method used for the LDH precursors [14] and the presence of a promoter and its content [15]. Notably, Cu-containing mixed oxides catalysts obtained from LDH precursors were also shown to be highly efficient for the complete oxidation of different VOC such as toluene [16,17], methanol and formic acid [18], ethanol [19], and propane [20].

Recently, it has been shown [21] that Ce-containing Cu-based LDH-derived mixed oxide catalysts are quite active in the total oxidation of methane, the optimum composition corresponding to a CuCeMgAlO

system with 15% Cu, 10% Ce (at.%, with respect to cations), and Mg/Al atomic ratio of 3. For this, an excellent dispersion of Cu in the CeMgAlO matrix was observed favoring a strong synergistic effect between Cu and Ce and, hence, an enhanced catalytic activity. Thus, taking into consideration previously reported results [22–26] showing an enhanced synergy effect between Cu and Ce in the presence of transition-metal cations M, such as Mn [22,24], Co [25], Ni [25], and Fe [26], the present work aimed to improve the catalytic performance of this LDH-derived CuCeMgAlO mixed oxide by promoting it with 3 at.% M, with M = Mn, Fe, Co, and Ni. For the best promoted catalyst in this series, the effect of the transition metal M content in the range from 1 to 9 at.% on the catalytic performance was also investigated.

2. Results and Discussion

2.1. Catalysts Characterization

The XRD patterns of the as-prepared M(3)CuCeMgAl and Co(x)CuCeMgAl LDH precursors are displayed in Figure 1. All the M(3)CuCeMgAl LDH precursors consisted of well-crystallized LDH phase (Powder Diffraction File (PDF) 37-0630) together with poorly crystallized boehmite AlOOH phase (PDF 83-2384) (Figure 1a). The M-free CuCeMgAl LDH precursor consisted of a mixture of both LDH and boehmite poorly crystallized phases (Figure 1a). The absence of diffraction lines corresponding to cerium- or transition metal-containing additional phases can be noted, suggesting that these cations were well dispersed in the M(3)CuCeMgAl LDH precursor samples, as already observed in CuCeMgAl LDH materials [27]. The Co(x)CuCeMgAl LDH precursors also consisted of a mixture of well-crystallized LDH and poorly crystallized boehmite AlOOH phases (Figure 1b). However, diffraction lines corresponding to CuO tenorite phase (PDF 41-0254) could be observed at higher Co contents, i.e., $x = 6$ and 9 at.%. This could be explained as follows: at high Co contents the M^{2+}/M^{3+} atomic ratio became higher than the upper limit corresponding to the LDH phase formation, i.e., $M^{2+}/M^{3+} = 4$, and, because of its pronounced Jahn–Teller effect, Cu^{2+} left the brucite-like layers, forming a separate phase to the benefit of Co^{2+} species, which entered the LDH layers [9].

The (110) and (003) reflections were used to calculate the lattice parameters a ($a = 2 \times d_{110}$) and c ($c = 3 \times d_{003}$), respectively, assuming a hexagonal symmetry for the LDH structure (Table 1). In both M(3)CuCeMgAl and Co(x)CuCeMgAl LDH series the values of the cell parameter a were close together, accounting for similar mean intermetallic distances in the layers. This suggests that the different cations were homogeneously distributed in the hydroxide layers. The cell parameter c , which is a function of different factors, like the nature of the interlayer anion, the average charge of the LDH layers, and the amount of water in the interlayer space, accounted for the presence of mainly nitrate as compensating anion [28], originating from the precursor salts used for the LDH synthesis.

Table 1. Cell parameters and crystallite size of the LDH precursors.

LDH Sample	a (nm)	c (nm)	Crystallite Size ^a (nm)
Mn(3)CuCeMgAl-LDH	0.306	2.420	10.3
Fe(3)CuCeMgAl-LDH	0.306	2.401	9.7
Co(3)CuCeMgAl-LDH	0.307	2.382	11.6
Ni(3)CuCeMgAl-LDH	0.306	2.389	10.1
Co(1)CuCeMgAl-LDH	0.307	2.371	11.8
Co(6)CuCeMgAl-LDH	0.307	2.393	11.9
Co(9)CuCeMgAl-LDH	0.307	2.392	12.2

^a Crystallite size in c direction as obtained from (003) reflection using the Debye–Scherrer equation.

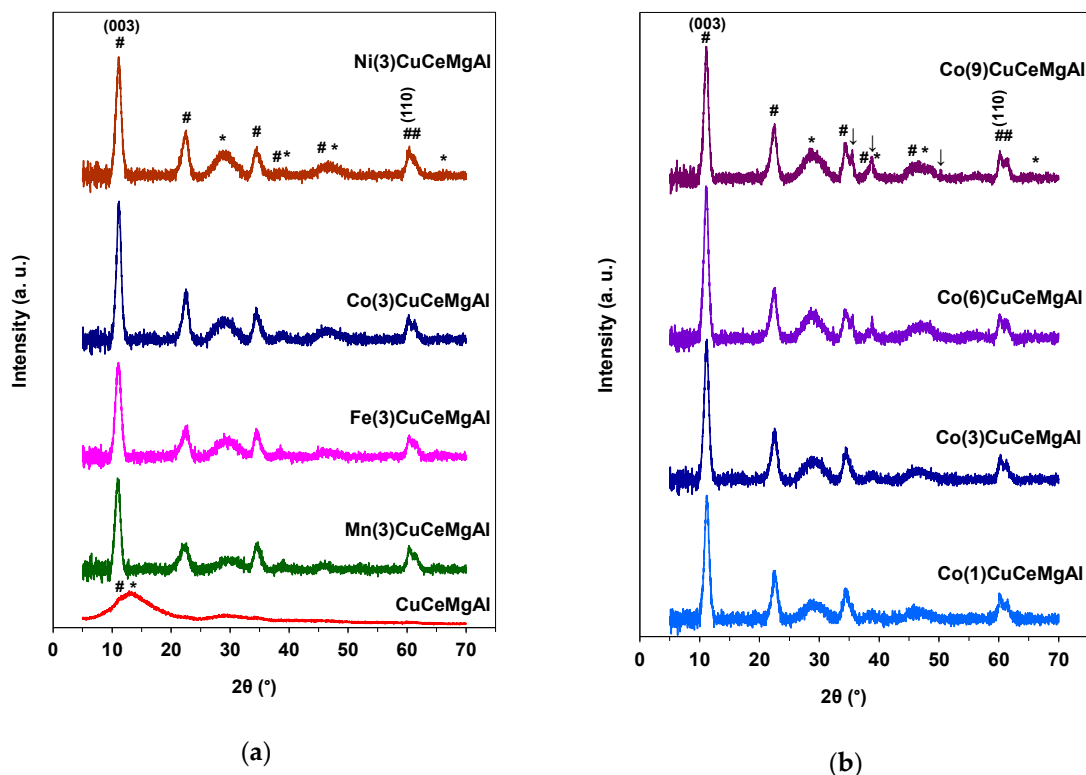


Figure 1. XRD patterns of (a) CuCeMgAl and M(3)CuCeMgAl, and (b) Co(x)CuCeMgAl LDH precursors. Symbols: #—LDH phase, *—boehmite (AlOOH) phase, ↓—CuO tenorite.

The mean crystallite size in the *c* direction (Table 1) was estimated from the full-width at half-maximum of the LDH (003) reflection by using the Debye-Scherrer equation. For both M(3)CuCeMgAl and Co(x)CuCeMgAl LDH precursors, nanometric crystallite sizes within the range 9.7–12.2 nm were observed.

The XRD patterns of the calcined M(3)CuCeMgAlO and Co(x)CuCeMgAlO mixed oxides are displayed in Figure 2. The periclase-like Mg(Al)O mixed oxide phase (PDF 04-0829) together with CeO₂ fluorite phase (PDF 75-0076) were identified in all the calcined mixed oxides. Except for CuCeMgAlO system, more or less intense diffraction lines attributed to CuO tenorite phase were observed in both M(3)CuCeMgAlO (Figure 2a) and Co(x)CuCeMgAlO (Figure 2b) mixed oxides, and, for the latter, their intensity increased with increasing the Co content. Obviously, adding transition metals M (M = Mn, Fe, Co, and Ni) to CuCeMgAlO composition and increasing their content determined the segregation of CuO tenorite phase.

The lattice parameters of the ceria fluorite structure were calculated using the Bragg's law from the three most intense (111), (220), and (311) reflections, and are presented in Table 2. It can be observed that they were all close together, i.e., $a = 0.5416 \pm 0.0002$ nm, and close to that corresponding to the M-free CuCeMgAlO sample (0.5415 nm). On the other hand, the lattice parameters of the periclase-like phase calculated from the (200) reflection at ca. $43^\circ 2\theta$ (Table 2) were close together for both M(3)CuCeMgAlO and Co(x)CuCeMgAlO mixed oxides, i.e., $a = 0.4215 \pm 0.0004$ nm, but were significantly higher than that of the M-free CuCeMgAlO sample (0.4201 nm). These data suggest that the cations M in both M(3)CuCeMgAlO and Co(x)CuCeMgAlO mixed oxides were homogeneously dispersed in the periclase-like Mg(Al)O phase rather than in the ceria phase. However, the existence of small quantities of poorly crystallized transition metal oxide-based side phases in the transition metal-promoted CuCeMgAlO mixed oxides could not be totally ruled out.

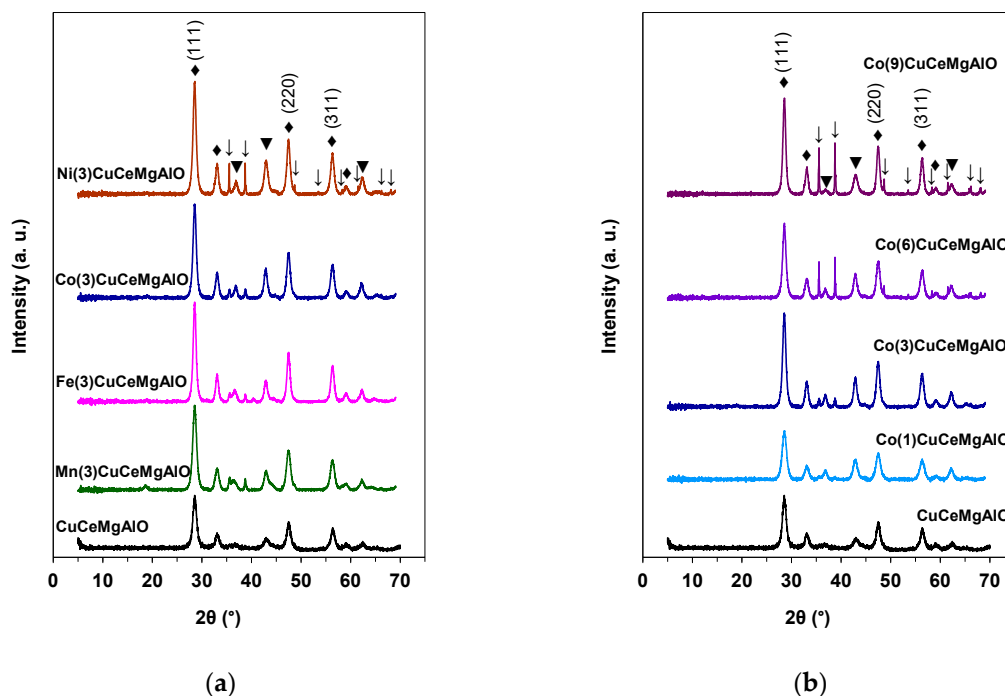


Figure 2. XRD patterns of (a) M(3)CuCeMgAlO and (b) Co(x)CuCeMgAlO mixed oxides calcined at 750 °C. Symbols: ↓—CuO tenorite phase. ◆—CeO₂ fluorite phase. ▼—Periclase-like Mg(Al)O mixed oxide phase.

Table 2. Crystallographic data of the LDH-derived mixed oxides.

Mixed Oxide Sample	CeO ₂ Lattice Parameter (nm)	CeO ₂ Crystallite Size (nm)	Mg(Al)O Lattice Parameter (nm)	Mg(Al)O Crystallite Size (nm)
CuCeMgAlO	0.5415	12.2	0.4201	10.1
Mn(3)CuCeMgAlO	0.5416	12.0	0.4215	12.7
Fe(3)CuCeMgAlO	0.5417	15.3	0.4216	15.2
Co(3)CuCeMgAlO	0.5417	14.1	0.4218	14.4
Ni(3)CuCeMgAlO	0.5418	14.5	0.4211	13.0
Co(1)CuCeMgAlO	0.5414	10.8	0.4219	12.5
Co(6)CuCeMgAlO	0.5415	13.6	0.4218	13.8
Co(9)CuCeMgAlO	0.5415	16.6	0.4212	12.3

The full-width at half-maximum (FWHM) of the three most intense (111), (220), and (311) diffraction lines of CeO₂ phase were used to calculate the mean crystallite size with the Debye–Scherrer equation:

$$D \approx \frac{1.08\lambda}{(2\theta)_{FWHM} \cos \theta}$$

where D is the crystallite size, λ is the wavelength of the Cu K-alpha radiation (0.15406 nm), and θ is the Bragg diffraction angle. They are presented in Table 2. It can be observed that the crystallite size of ceria varied in the range of 13.7 ± 2.9 nm. The Debye–Scherrer equation was also used to calculate the mean crystallite size of the periclase-like phase from the two most intense reflections at ca. 43 and 62° 2 θ (Table 2). The crystallite size of the solid solution periclase-like phase was similar for all the transition metal-promoted CuCeMgAlO mixed oxides, i.e., $D = 13.8 \pm 1.5$ nm, being higher than that observed for the M-free CuCeMgAlO system.

The decomposition of the LDH precursors into their corresponding mixed oxides has been followed by thermogravimetric and differential thermal analyses. The TG curves of selected LDH precursors are presented in Figure S1, while the TG-DTG-DTA curves of the as-prepared Co(3)CuCeMgAl LDH precursor, representative of all samples, are presented in Figure 3. They are characteristic for the LDH materials [29] with two weight losses. The first weight loss of 9–13% (with DTG-DTA peaks at 110 and 170 °C for the Co(3)CuCeMgAl LDH precursor) was ascribed to the removal of weakly bounded and interlayered water molecules, while the second weight loss in the range of 20–24% (with DTG-DTA peaks at 350 and 395 °C for Co(3)CuCeMgAl LDH) was attributed to the dehydroxylation of the LDH layers and the decomposition of the anions from the interlayer space.

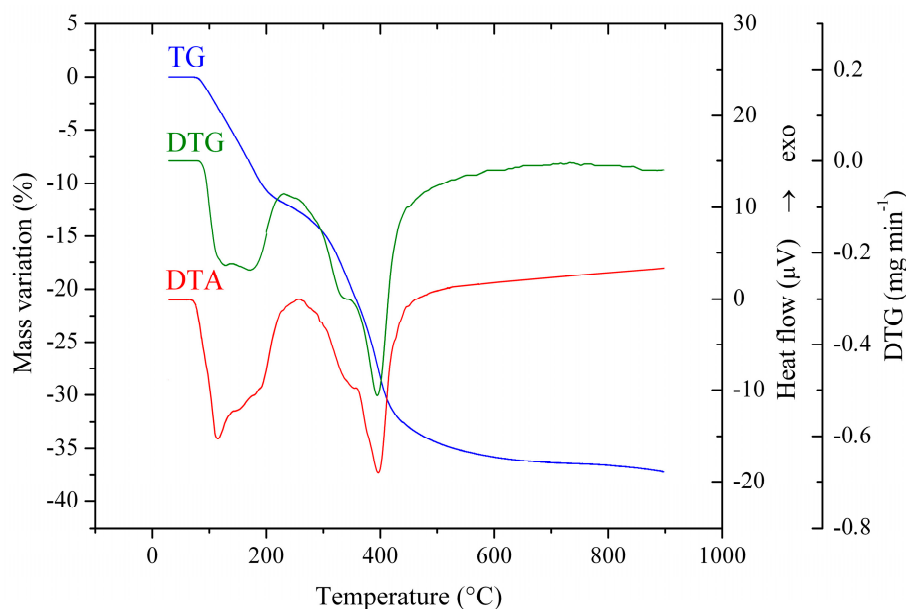


Figure 3. TG-DTG-DTA curves of the Co(3)CuCeMgAl LDH precursor.

The structure and morphology of the LDH-derived mixed oxides were further studied via transmission electron microscopy (TEM) and scanning electron microscopy (SEM). The TEM images of selected mixed oxides (Figure S2) revealed that they have a scale-like structure with nanoparticle sizes of ca. 5–15 nm. Regular and smooth lattice fringes could also be observed, confirming the good crystallinity of the materials. The SEM images of all the mixed oxides are displayed in Figure S3. All the images show agglomerated powders with micro- and nanometric features that generated a large surface area. Notably, in powders with a higher Co content, crystalline, rectangular, parallel-piped shapes of different sizes were observed. These corresponded to copper oxides with tenorite structure [30], in good agreement with the conclusions drawn from the XRD analysis.

The cationic composition of the calcined mixed oxide catalysts was determined by EDX spectroscopy and it is tabulated in Table 3. It can be observed that, for all the samples, the cationic content was close to the calculated values within the limits of experimental error of the method used, except for Mn(3)- and Fe(3)CuCeMgAlO samples, for which it was slightly more different. The Mg/Al and Cu/Ce atomic ratios varied in the ranges 3.0–3.3 and 1.5–1.7, respectively, being thus close to the fixed values of 3 and 1.5, respectively, except for Mn(3)CuCeMgAlO sample, for which they were slightly higher, i.e., 3.5 and 2.1, respectively.

Table 3. Cationic composition of the calcined oxide catalysts estimated by EDX spectroscopy.

Mixed Oxide	Atomic Content (% with Respect to Cations)					Atomic Ratio	
	M	Cu	Ce	Mg	Al	Mg/Al	Cu/Ce
CuCeMgAlO	-	17.2	10.8	54.0	18.1	3.0	1.6
Mn(3)CuCeMgAlO	2.2	20.7	9.9	52.4	14.8	3.5	2.1
Fe(3)CuCeMgAlO	4.1	19.4	11.4	49.3	15.8	3.1	1.7
Co(3)CuCeMgAlO	3.1	14.0	8.9	56.4	17.5	3.2	1.6
Ni(3)CuCeMgAlO	2.7	13.1	8.9	56.7	18.6	3.0	1.5
Co(1)CuCeMgAlO	0.7	13.3	8.5	59.1	18.4	3.2	1.6
Co(6)CuCeMgAlO	6.2	16.2	10.5	51.7	15.6	3.3	1.5
Co(9)CuCeMgAlO	8.9	13.4	8.7	52.9	16.1	3.3	1.5

The surface composition of both M(3)CuCeMgAlO and Co(x)CuCeMgAlO mixed oxides together with the oxidation states of the different elements were studied by X-ray photoelectron spectroscopy (XPS). All the expected cations together with oxygen and carbon were evidenced on the surface of the different oxides, their respective content being tabulated in Table S1. For all the mixed oxides the O 1s core level XPS spectra (Figure 4a) consisted of a peak deconvoluted into two components at ca. 529.7 and 531.6 eV, which were ascribed to lattice oxygen in oxide and oxygen in the lateral structure, respectively [31]. The oxygen in the lateral structure was associated to hydroxyl and/or carbonate species [32] and also to subsurface oxygen ions with particular coordination and lower electron density than the lattice oxygen probably located at the interface of the crystalline CuO and CeO₂ phases [21,31].

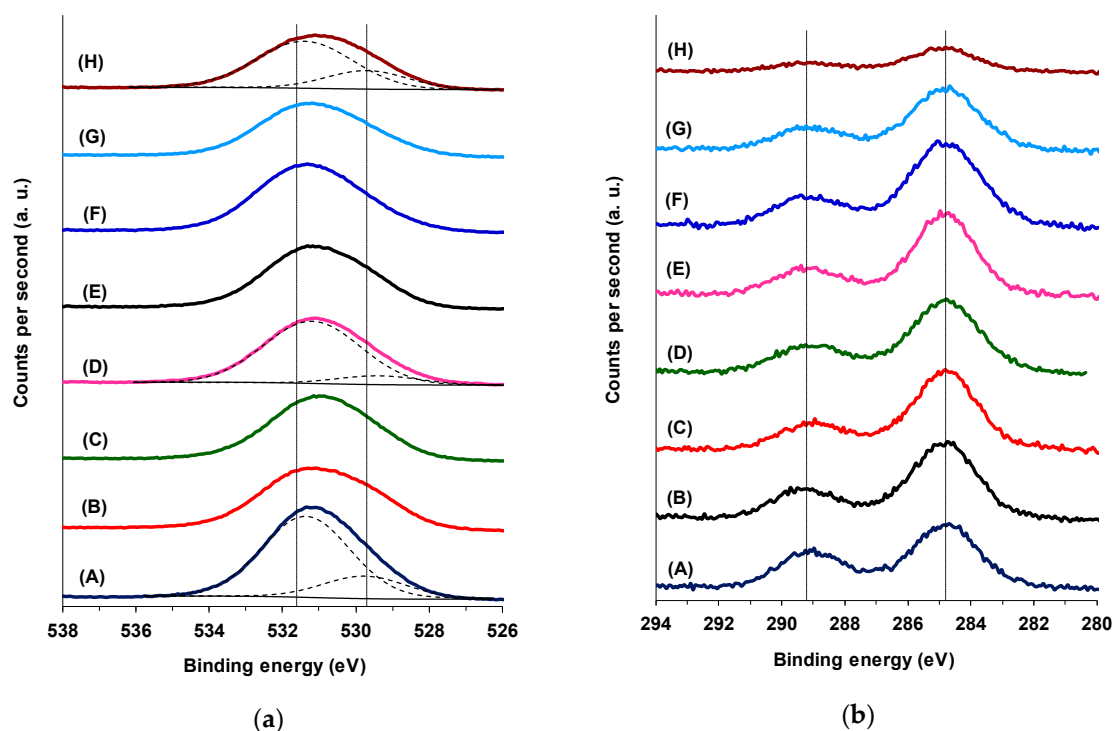


Figure 4. (a) O 1s core level and (b) C 1s core level XPS spectra of the mixed oxides: CuCeMgAlO (A), Mn(3)CuCeMgAlO (B), Fe(3)CuCeMgAlO (C), Co(3)CuCeMgAlO (D), Ni(3)CuCeMgAlO (E), Co(1)CuCeMgAlO (F), Co(6)CuCeMgAlO (G), Co(9)CuCeMgAlO (H).

The C 1s core level XPS spectra (Figure 4b) showed two main contributions at 284.8 and ca. 289.2 eV attributed to adventitious hydrocarbon species and carbon in carbonate, respectively [32]. This confirmed the need of a thermal treatment of the LDH-derived catalysts in the reactor before each activity test in order to clean their surface [33].

Figure 5 shows the photoelectron profile of Cu 2p region for both M(3)CuCeMgAlO and Co(x)CuCeMgAlO mixed oxides, while in Table 4 are presented the surface concentrations of copper together with Cu²⁺/Cu atomic ratios. Cu 2p_{3/2} emission with two components centered at 932.2 and 934.2 eV was observed in all the mixed oxides, indicating the presence of both Cu⁺ and Cu²⁺ surface species, respectively [34,35]. The shake-ups of Cu 2p_{3/2} emission line, centered at 941.2 and 943.7 eV, confirmed the presence of surface Cu²⁺ as well [35]. The presence of Cu⁺ surface species in the mixed oxides suggests that, at least at the interface, CuO phase could be doped with higher valence cations, such as M³⁺, Al³⁺, and/or Ce⁴⁺, existing in the mixed oxide.

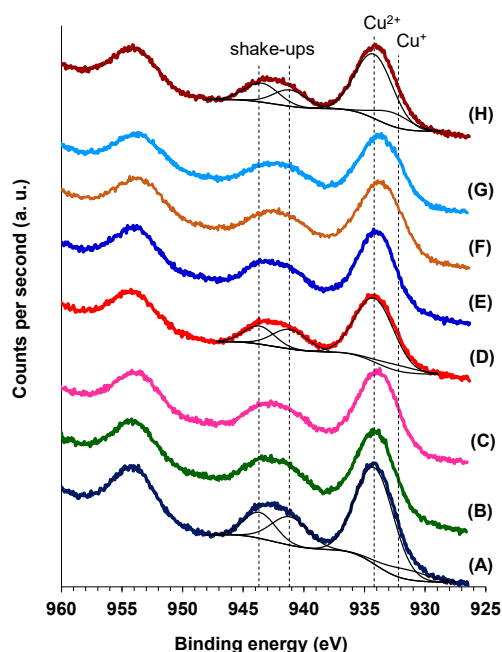


Figure 5. Cu 2p core level XPS spectra of the mixed oxides: CuCeMgAlO (A), Mn(3)CuCeMgAlO (B), Fe(3)CuCeMgAlO (C), Co(3)CuCeMgAlO (D), Ni(3)CuCeMgAlO (E), Co(1)CuCeMgAlO (F), Co(6)CuCeMgAlO (G), Co(9)CuCeMgAlO (H).

The data in Table 4 show that, except for Mn(3)- and Fe(3)CuCeMgAlO, the surface of the catalysts was enriched in Cu compared to the bulk composition (Table 3). The Cu²⁺/Cu surface atomic ratio was calculated by the method developed in [35] using the following equation:

$$\%Cu^{2+} = \frac{B(1 + (A1_s/B_s))}{A + B} \times 100$$

where A is the total area of the main Cu 2p_{3/2} emission line, B is the area of the shake-up peak, and $A1_s/B_s$ is a factor representing the ratio between the area of the main peak and that of the shake-up peak for a sample containing only Cu²⁺ which is equal to 1.89 ± 0.08 for 20 eV pass energy [35]. The surface Cu²⁺/Cu atomic ratio varied in the range from 0.76 to 0.92, being lower for both M(3)CuCeMgAlO and Co(x)CuCeMgAlO mixed oxides compared to the unpromoted CuCeMgAlO, except for Co(3)CuCeMgAlO. This shows that,

except for the last, the amount of surface Cu^+ species was higher in the promoted catalysts compared to the unpromoted one.

Table 4. Surface cationic composition of the mixed oxide catalysts determined by XPS analysis ^a.

Sample	Surface Cationic Content (at.%)					Surface Atomic Ratios					
	M	Cu	Ce	Mg	Al	$\frac{M}{Cu}$	$\frac{Cu}{Ce}$	$\frac{Mg}{Al}$	$\frac{M^{n+}}{M^{(n-1)+}}$ ^b	$\frac{Cu^{2+}}{Cu}$	$\frac{Ce^{4+}}{Ce}$
CuCeMgAlO	-	19.8	5.2	51.2	23.8	-	3.8	2.2	-	0.90	0.93
Mn(3)CuCeMgAlO	3.8	15.6	8.0	53.9	18.5	0.25	1.9	2.9	0.67	0.87	0.88
Fe(3)CuCeMgAlO	2.9	17.9	5.1	55.4	18.8	0.15	3.5	2.9	0.46	0.85	0.80
Co(3)CuCeMgAlO	5.4	16.7	5.8	51.3	20.9	0.33	3.0	2.5	0.40	0.92	0.91
Ni(3)CuCeMgAlO	7.5	17.4	7.8	48.1	19.2	0.43	2.3	2.5	-	0.85	0.88
Co(1)CuCeMgAlO	3.2	15.7	4.3	53.5	23.2	0.20	3.4	2.3	0.27	0.76	0.79
Co(6)CuCeMgAlO	8.3	16.3	5.0	46.9	23.3	0.52	3.3	2.0	0.22	0.81	0.88
Co(9)CuCeMgAlO	11.1	18.9	5.8	43.1	21.0	0.58	3.1	2.0	0.20	0.83	0.87

^a Reference binding energy: C1s = 284.8 eV. ^b For M = Mn: $\text{Mn}^{4+}/\text{Mn}^{3+}$; for M = Fe: $\text{Fe}^{3+}/\text{Fe}^{2+}$; for M = Co: $\text{Co}^{3+}/\text{Co}^{2+}$; and for M = Ni: Ni^{2+} only.

The X-ray photoelectron spectra of the Ce 3d_{3/2} and Ce 3d_{5/2} core levels of both M(3)CuCeMgAlO and Co(x)CuCeMgAlO mixed oxides are presented in Figure 6. It can be observed that all the XPS spectra show 10 peaks, suggesting that both Ce³⁺ and Ce⁴⁺ species were present on the surface of all the mixed oxides. Indeed, six peaks corresponding to three pairs of spin-orbit doublets, conventionally labeled in order of decreasing energy U''', U'', U (for Ce 3d_{3/2}) and V''', V'', V (for Ce 3d_{5/2}), were attributed to Ce⁴⁺ species, while four peaks corresponding to two pairs of spin-orbit doublets, labeled U', U⁰ (for Ce 3d_{3/2}) and V', V⁰ (for Ce 3d_{5/2}), were attributed to Ce³⁺ species [36]. Their characteristic binding energies were taken from [37]. The U''' peak was not observed in the Ce 3d spectrum of a pure Ce³⁺ oxide, being exclusively attributed to Ce⁴⁺ species. Therefore, it was used as a quantitative measure of the amount of Ce⁴⁺ [38]. Thus, taking into consideration that for pure CeO₂ the U''' peak represented ca. 14% of total integral intensity [38], the surface Ce⁴⁺ content was calculated using the following equation:

$$\%Ce^{4+} = \frac{\%U'''}{14} \times 100$$

where %U''' represents the percentage of U''' peak area with respect to the total Ce 3d area. The Ce⁴⁺/Ce surface atomic ratio thus calculated is tabulated in Table 4. It varied in the range from 0.79 to 0.93, being lower for both M(3)CuCeMgAlO and Co(x)CuCeMgAlO mixed oxides compared to the unpromoted CuCeMgAlO. This shows that the amount of surface Ce³⁺ species was higher in the promoted catalysts compared to the unpromoted one, in agreement with previously reported results for co-doped CeO₂ [23]. Moreover, the Ce⁴⁺/Ce surface atomic ratio roughly parallels the Cu²⁺/Cu surface atomic ratio (Figure S4) for both M(3)CuCeMgAlO and Co(x)CuCeMgAlO series of mixed oxides, suggesting that the promoter equally favored the reduction of both Ce⁴⁺ and Cu²⁺ surface species in the promoted catalysts and, hence, improved the synergistic effect between Cu and Ce [23]. It is worth noting that responsible for the presence of surface Ce³⁺ species was, at least partly, the reduction of Ce⁴⁺ under the X-ray beam during the XPS analysis. The data in Table 4 also show that the surface concentration of cerium was lower than its bulk concentration (Table 3) for all the mixed oxides and, except for the Mn(3)CuCeMgAlO sample, the Cu/Ce surface atomic ratio (Table 4) was significantly higher than the bulk ratio (Table 3).

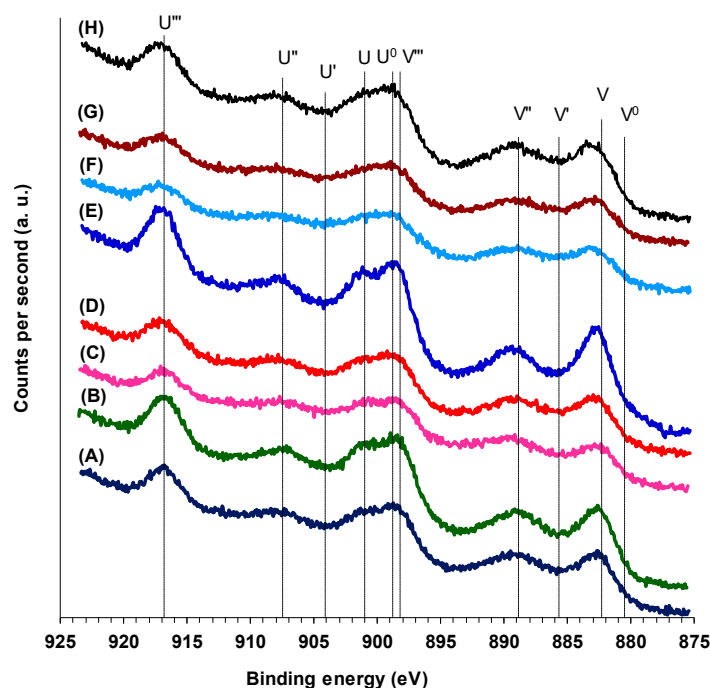


Figure 6. Ce 3d core levels XPS spectra of the mixed oxides: CuCeMgAlO (A), Mn(3)CuCeMgAlO (B), Fe(3)CuCeMgAlO (C), Co(3)CuCeMgAlO (D), Ni(3)CuCeMgAlO (E), Co(1)CuCeMgAlO (F), Co(6)CuCeMgAlO (G), Co(9)CuCeMgAlO (H).

The Al 2p and Mg 2p X-ray photoelectron spectra of all the mixed oxides are shown in Figures S5 and S6, respectively. Figure S6 also shows their Auger Mg KLL spectra. Although the Al 2p peak appeared at almost the same binding energy as Cu 3p, the deconvolution of the XPS signal allowed us to unambiguously identify and quantify it. The relative peak positions of both Al and Mg were very stable (Table S2) and accounted for Al³⁺ and Mg²⁺ in their corresponding oxides. This was confirmed for Mg by calculating the modified Auger parameter (*m-AP*) using the following formula:

$$m - AP = BE_{Mg2p} + KE_{MgKLL}$$

where BE_{Mg2p} is the binding energy of Mg 2p and KE_{MgKLL} , the kinetic energy of the Mg KLL peak. Indeed, the values obtained for *m-AP* (Table S2) were specific for MgO [39] in all the mixed oxide samples. The Mg/Al surface atomic ratio (Table 4) was lower than the bulk ratio for all the mixed oxides studied, indicating an Al enrichment of the surface.

The photoelectron profiles of Mn 2p, Fe 2p, and Ni 2p of the Mn(3)-, Fe(3)-, and Ni(3)CuCeMgAlO mixed oxides, respectively, are shown in Figure S7, while their corresponding surface concentrations are tabulated in Table 4. Each emission line (2p_{3/2} and 2p_{1/2}) of the X-ray photoelectron spectrum of Mn 2p was fitted with three peaks corresponding to Mn³⁺, Mn⁴⁺, and a shake-up [40]. The 2p_{3/2} components at 641.7 and 643.3 eV attributed to Mn³⁺ and Mn⁴⁺, respectively, were used to calculate the Mn⁴⁺/Mn³⁺ surface ratio, which was equal to 0.67. The photoelectron spectrum of Fe 2p showed the presence of both Fe²⁺ and Fe³⁺ species on the surface of the Fe(3)CuCeMgAlO mixed oxide. The Fe³⁺/Fe²⁺ surface ratio was found to be 0.46. The observed Ni 2p photoelectron spectrum corresponded to hydroxylated nickel oxide [41]. The Ni 2p_{3/2} emission line and its shake-up peak centered at 856 and 861.9 eV, respectively, were attributed to high spin Ni²⁺ species [42,43]. The surface concentrations of Mn and Ni were higher, while that of Fe was lower (Table 4) compared to their corresponding bulk concentrations (Table 3).

Figure 7 shows the photoelectron profiles of Co 2p region for the Co(x)CuCeMgAlO mixed oxides, while in Table 4 are presented the surface concentrations of cobalt. The photoelectron spectra were deconvoluted into two spin-orbit doublets corresponding to Co^{3+} and Co^{2+} species, respectively, and two shake-up peaks [44]. Thus, the Co $2p_{3/2}$ component at 780.0 eV and a $2p_{3/2}$ – $2p_{1/2}$ splitting of ca. 15.3 eV was attributed to Co^{3+} species, while that at 781.4 eV and a $2p_{3/2}$ – $2p_{1/2}$ splitting of ca. 15.4 eV was attributed to Co^{2+} species. The surface $\text{Co}^{3+}/\text{Co}^{2+}$ atomic ratios are presented in Table 4. It can be observed that the $\text{Co}^{3+}/\text{Co}^{2+}$ surface ratio passes through a maximum with increasing the Co content in the Co(x)CuCeMgAlO series, which corresponded to the Co(3)CuCeMgAlO system. The data in Table 4 also show that the surface of all the Co-promoted mixed oxides was enriched in Co compared to the bulk composition (Table 3).

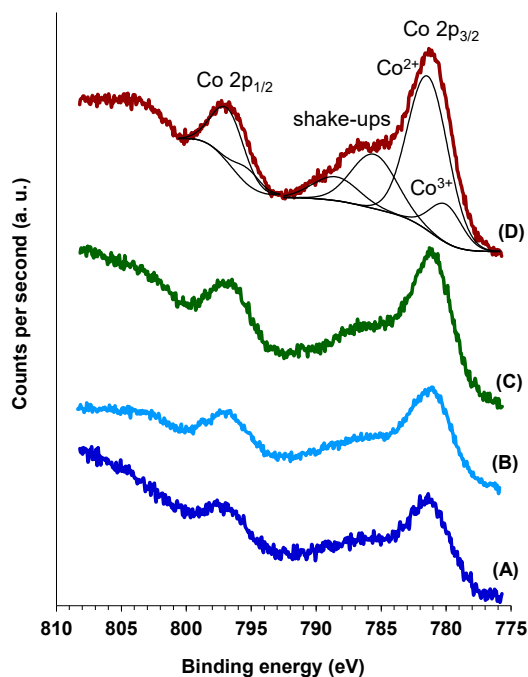


Figure 7. The X-ray photoelectron profiles of Co 2p for the Co(x)CuCeMgAlO mixed oxides: (A) $x = 1$, (B) $x = 3$, (C) $x = 6$, and (D) $x = 9$.

The electronic spectra of all the transition metal-promoted CuCeMgAlO mixed oxides (Figure 8) contained both charge transfer (CT) bands and d-d transition bands. The strong bands in the ultraviolet range are characteristic to charge transfer transitions between copper and oxygen ions [45]. The spectra of all the investigated materials showed two absorption maxima in this region at ca. 260 and 320 nm, which were assigned to CT bands characteristic for mononuclear Cu^{2+} centers and oligomeric species $(\text{Cu}^{2+}-\text{O}^{2-}-\text{Cu}^{2+})_n^{2+}$, respectively [21,46]. The weak bands from the visible range (ca. 625–670 nm) were attributed to $d_{z^2} \rightarrow d_{x^2-y^2}$ transitions characteristic for Cu^{2+} ion in an octahedral stereochemistry [45]. Moreover, for cobalt-containing oxides, new bands appeared in the near-infrared region of the spectra as the cobalt content increased. These bands were assigned to ${}^4\text{T}_{1g} \rightarrow {}^4\text{A}_{2g}$ (910 nm) and ${}^4\text{T}_{1g} \rightarrow {}^4\text{T}_{2g}$ (1220 nm) transitions, which are characteristic for Co^{2+} ion in an octahedral stereochemistry [45]. This was in line with the dispersion of cobalt species in the periclase-like Mg(Al)O phase, as suggested by the XRD analysis.

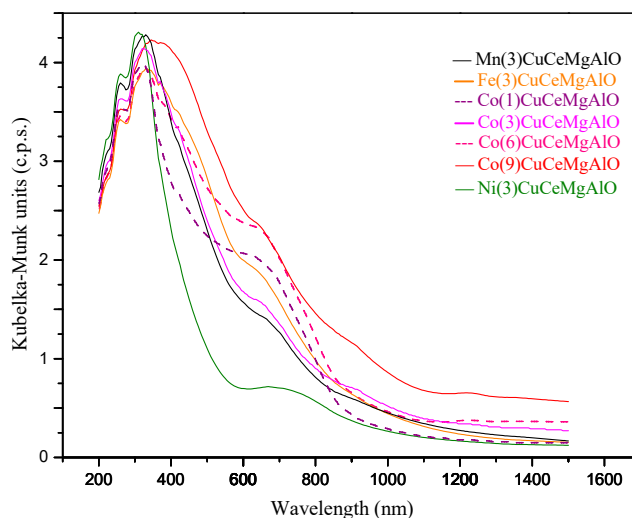


Figure 8. Electronic spectra of the transition metal-promoted CuCeMgAlO mixed oxide catalysts.

The adsorption-desorption isotherms of the unpromoted and transition metal-promoted CuCeMgAlO mixed oxides are shown in Figure S8. All the solids revealed type IV isotherms with either H3-type or a combination of H3 with H2b types hysteresis loops specific for mesoporous materials with either slit-shaped pores or more complex pore structures [47]. The specific surface areas (Table 5) of all the transition metal-promoted CuCeMgAlO samples were close together and, for the Co(x)CuCeMgAlO mixed oxides, varied irrespective of the Co content, in line with their similar particle sizes of the periclase-like phase ($D = 13.8 \pm 1.5$ nm). However, their specific surface area was lower than that of the unpromoted CuCeMgAlO mixed oxide, in line with its lower particle size of the periclase-like phase ($D = 10.1$ nm).

Table 5. Textural properties of the LDH-derived mixed oxides.

Mixed Oxide	Surface Area ($\text{m}^2 \text{g}^{-1}$)	Pore Volume ($\text{cm}^3 \text{g}^{-1}$)	Pore Size ^a (nm)
CuCeMgAlO	120.0	0.23	3.7 and 11.4
Mn(3)CuCeMgAlO	72.0	0.29	9.0
Fe(3)CuCeMgAlO	62.4	0.17	9.2
Co(3)CuCeMgAlO	69.8	0.25	8.8
Ni(3)CuCeMgAlO	77.6	0.35	7.4
Co(1)CuCeMgAlO	68.5	0.23	9.0 and 15.2 ^b
Co(6)CuCeMgAlO	67.7	0.25	10.8
Co(9)CuCeMgAlO	66.0	0.21	10.7

^a Maxima of pore size distribution. ^b Shoulder.

The pore volume of all mixed oxides varied in the range of $0.17 \text{ cm}^3 \text{g}^{-1}$ for Fe(3)CuCeMgAlO to $0.35 \text{ cm}^3 \text{g}^{-1}$ for Ni(3)CuCeMgAlO (Table 5). The pore size distributions of the mixed oxides (Figure S9) obtained from the desorption branch of isotherms indicated unimodal pore structures extending from 2 to ca. 20 nm, with well-defined maxima ranging from 7.4 nm for Ni(3)CuCeMgAlO to 10.8 nm for Co(6)CuCeMgAlO (Table 5). A shoulder at 15.2 nm was also noticed in the pore size distribution of the Co(1)CuCeMgAlO sample. For the M-free CuCeMgAlO sample a well-defined bimodal pore size distribution with maxima at 3.7 and 11.4 could be observed.

The reduction behavior of the different mixed oxides was investigated by H_2 -TPR measurements, their reduction profiles being displayed in Figure 9 with the corresponding H_2 consumptions tabulated in Table 6. For the unpromoted CuCeMgAlO system, only one broad and intense reduction peak was

observed in the temperature range 125–390 °C, with a tail extending up to 550 °C. This TPR profile accounted for the reduction of both Cu^{2+} and Ce^{4+} species, as described elsewhere [21]. Thus, the broad and intense reduction peak with several maxima below 390 °C was attributed to the successive reduction of Cu^{2+} species doped in the ceria particles, from well-dispersed and sintered CuO particles interacting more or less strongly with the CeMgAlO support and to the reduction of Ce^{4+} species from highly reducible smaller ceria particles, while the tail was attributed to the reduction of Ce^{4+} species from less reducible larger ceria particles [21]. The hydrogen spillover on the metallic Cu particles was likely involved in the reduction of surface ceria lowering its reduction temperature [48]. It is worth noting that the reduction model of small and large ceria particles is equivalent with that of surface and bulk ceria, often used to explain the reduction profile of Ce -containing materials, as small and large particles are mostly surface and mostly bulk, respectively [48].

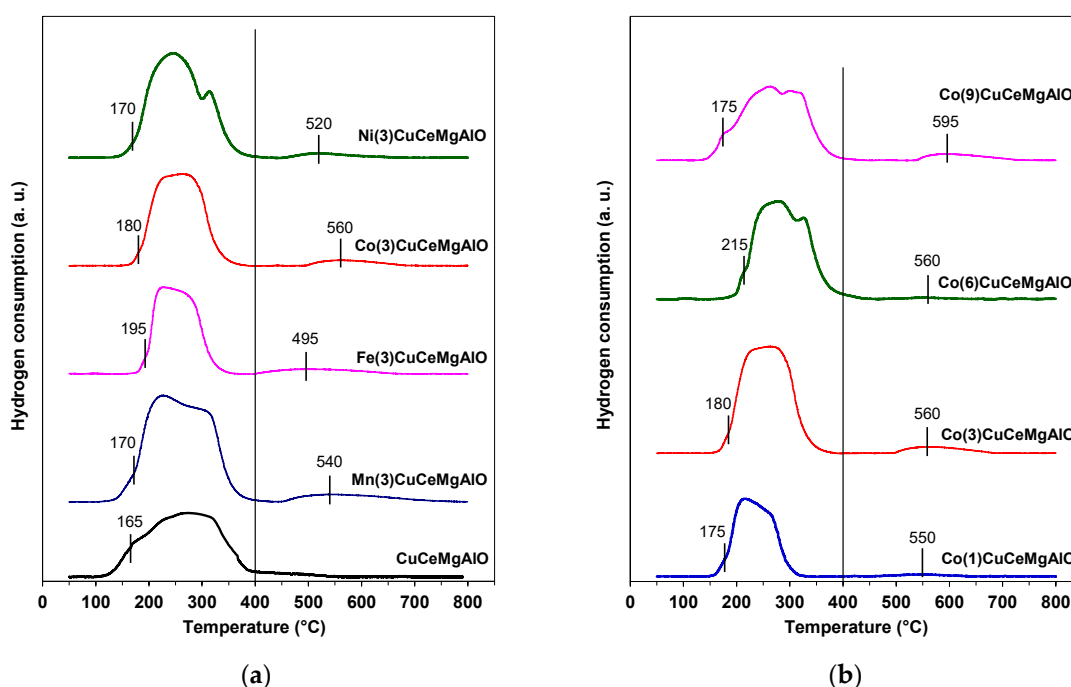


Figure 9. H_2 -TPR profiles of (a) CuCeMgAlO and $\text{M}(3)\text{CuCeMgAlO}$ and (b) $\text{Co}(x)\text{CuCeMgAlO}$ mixed oxides.

Table 6. Hydrogen consumptions in the H_2 -TPR experiments.

Catalyst	H_2 Consumption (mmol g^{-1})			
	Low-Temperature Peak	High-Temperature Peak	Total	Necessary for Cu Reduction ^a
CuCeMgAlO	2.84	-	2.84	2.73
$\text{Mn}(3)\text{CuCeMgAlO}$	3.87	0.34	4.21	3.25
$\text{Fe}(3)\text{CuCeMgAlO}$	2.07	0.20	2.27	2.94
$\text{Co}(3)\text{CuCeMgAlO}$	2.57	0.16	2.73	2.31
$\text{Ni}(3)\text{CuCeMgAlO}$	3.20	0.11	3.31	2.19
$\text{Co}(1)\text{CuCeMgAlO}$	1.46	0.05	1.51	2.26
$\text{Co}(6)\text{CuCeMgAlO}$	2.48	0.03	2.51	2.50
$\text{Co}(9)\text{CuCeMgAlO}$	2.29	0.16	2.45	2.15

^a Calculated based on the oxide composition and assuming the total reduction of all copper species.

Due to the different nature of the transition-metal cations and the degree of crystallinity of the phases present, different reducibilities were expected for the M(3)CuCeMgAlO mixed oxides. Their H₂-TPR patterns showed an intense and broad peak in the low-temperature region, which was narrower compared to that of the M-free CuCeMgAlO mixed oxide and clearly ended at a temperature lower than 400 °C. A weak reduction peak at higher temperatures was also observed. The first reduction peak was due to the same reduction processes as observed for the M-free CuCeMgAlO system combined with the reduction of the transition-metal cations M. The latter promoted the redox ability of the material, resulting in sharp and overlapping peaks, in agreement with previously reported results [22]. The high-temperature weak peak can be attributed to the reduction of either Ce⁴⁺ species from less reducible larger ceria particles [48] or Mⁿ⁺ transition-metal ions from spinel-like phases with different stoichiometries [11]. Although the latter were not evidenced by X-ray diffraction, their presence could not be totally ruled out. The first maximum reduction temperature for the M(3)CuCeMgAlO systems was higher than that observed for the M-free CuCeMgAlO mixed oxide. This was obviously due to the significantly higher surface area of the latter [49]. Based on their first maximum reduction temperature, the reducibility of the M(3)CuCeMgAlO mixed oxides, in terms of easiness of reduction, increased as follows: Fe(3)CuCeMgAlO < Co(3)CuCeMgAlO < Mn(3)CuCeMgAlO ≈ Ni(3)CuCeMgAlO. This order corresponds to the decrease of the crystallite size of the Mg(Al)O periclase-like phase (Table 2), suggesting that the surface transition-metal species dispersed in the Mg(Al)O matrix determined the easiness of reduction of the studied mixed oxides. In terms of hydrogen consumption, their reducibility followed the order: Fe(3)CuCeMgAlO < Co(3)CuCeMgAlO < Ni(3)CuCeMgAlO < Mn(3)CuCeMgAlO. Notably, the hydrogen consumption for the Fe(3)CuCeMgAlO mixed oxide was lower than that necessary for the reduction of all the Cu species calculated based on the oxide composition (Table 6), suggesting that, for this mixed oxide, Cu was not quantitatively reduced, likely due to a hindered access of hydrogen to the reducible species, as reported earlier [11].

In the Co(x)CuCeMgAlO series, the low-temperature intense peak represented the overlap of the reduction of copper and highly reducible cerium species, as described above, with the reduction of cobalt species, its broadness going increasingly with increasing the Co content. Interestingly, the temperature maximum of the weak high-temperature reduction peak increased with increasing the CeO₂ crystallite size (Table 2), suggesting that it could be attributed to the reduction of Ce⁴⁺ species from less reducible larger ceria particles rather than to the reduction of Mⁿ⁺ transition-metal ions from spinel-like phases. Indeed, it was shown that the high-temperature reduction of ceria strongly depended on its crystallinity: the higher the crystallite size, the higher the reduction temperature [46]. In terms of easiness of reduction, the reducibility of the Co(x)CuCeMgAlO mixed oxides increased in the order Co(6)CuCeMgAlO < Co(3)CuCeMgAlO < Co(1)CuCeMgAlO ≈ Co(9)CuCeMgAlO, which corresponded to the decrease of the crystallite size of the Mg(Al)O periclase-like phase (Table 2), as observed for the M(3)CuCeMgAlO series. In terms of hydrogen consumption, the reducibility followed the order: Co(1)CuCeMgAlO < Co(9)CuCeMgAlO ≤ Co(6)CuCeMgAlO < Co(3)CuCeMgAlO. Unexpectedly, the hydrogen consumption did not increase with increasing the Co content, suggesting that the transition-metal species were decorated with non-reducible Mg(Al)O mixed oxide, which diminished the accessibility of hydrogen [11]. This was in line with both the XRD analysis and the UV-VIS spectroscopy data showing that the cobalt cations were homogeneously dispersed in the Mg(Al)O periclase-like phase. This was also supported by the XRD analysis of the Co(x)CuCeMgAl LDH precursors, showing that Co replaced Cu in the brucite-like layers for Co contents higher than 3 at.%, obviously leading to Mg(Al,Co)O periclase-like particles and segregated CuO after calcination. Thus, together with the CuO particles, only the cobalt species on the surface of the Mg(Al,Co)O periclase-like particles were reduced (the smaller the particle size, the easier the reduction), while those located in the bulk were not. Notably, in agreement with this, the hydrogen consumption for the Co(1)CuCeMgAlO mixed oxide was lower than that needed for the reduction of all the Cu species calculated based on the oxide composition (Table 6). Indeed, at low Co

content, when Cu remained in the brucite-like layers of the LDH precursor, both Co and Cu species were dispersed in the Mg(Al)O matrix of the calcined oxide and, hence, the reduction of the transition-metal species located in the bulk was prevented.

2.2. Catalytic Properties

The catalytic performance of the mixed oxide catalysts was evaluated in the complete oxidation of methane as a model molecule and compared to that of a reference Pd/Al₂O₃ catalyst previously reported in [14], with the light-off curves obtained being presented in Figure 10. As a measure of the catalytic activity, the temperatures corresponding to 10, 50, and 90% methane conversion (T_{10} , T_{50} , and T_{90} , respectively), together with the intrinsic and specific activities at 400 °C, are listed in Table 7. The light-off curve for Pd/Al₂O₃ catalyst, characterized by relatively low T_{50} and T_{90} values of 419 and 484 °C, respectively, accounted for its high activity in methane complete oxidation.

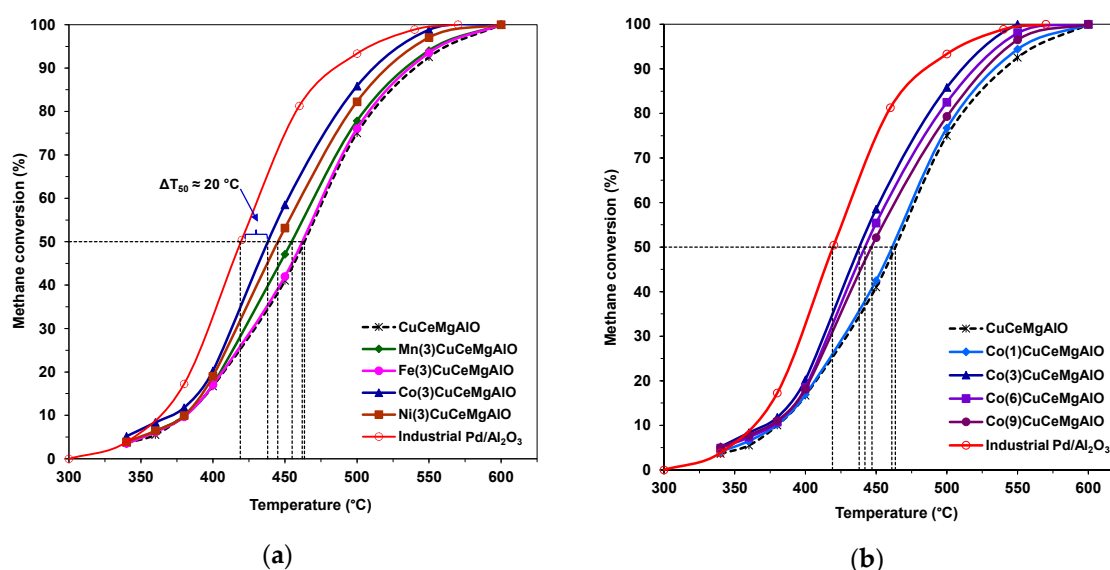


Figure 10. The light-off curves for the combustion of methane over (a) M(3)CuCeMgAlO and (b) Co(x)CuCeMgAlO mixed oxide catalysts compared with that of a reference Pd/Al₂O₃ catalyst. Reaction conditions: 1 vol.% CH₄ in air, GHSV of 16,000 h⁻¹, 1 cm³ of catalyst.

Table 7. Catalytic performance in the total oxidation of methane of the LDH-derived mixed oxides.

Catalyst	T_{10} (°C)	T_{50} (°C)	T_{90} (°C)	Reaction Rate at 400 °C		E_a (kJ mol ⁻¹)
				Specific (10 ⁷ mol g ⁻¹ s ⁻¹)	Intrinsic (10 ⁹ mol m ⁻² s ⁻¹)	
CuCeMgAlO	380	463	540	3.4	2.9	76.4
Mn(3)CuCeMgAlO	380	455	533	3.5	4.9	87.1
Fe(3)CuCeMgAlO	380	462	536	3.4	5.5	83.6
Co(3)CuCeMgAlO	372	438	511	4.2	6.0	81.4
Ni(3)CuCeMgAlO	380	445	521	3.9	5.0	88.6
Co(1)CuCeMgAlO	379	461	533	3.5	5.1	73.6
Co(6)CuCeMgAlO	377	442	520	3.8	5.6	82.2
Co(9)CuCeMgAlO	375	447	527	3.7	5.6	78.7

The light-off curves of both M(3)CuCeMgAlO and Co(x)CuCeMgAlO catalysts were between those of Pd/Al₂O₃ and M-free CuCeMgAlO, indicating, on one hand, that all the transition-metal M (M = Mn, Fe, Co, Ni) cations had a promoting effect on the CuCeMgAlO system, and, on the other hand, that this promoting effect depended on the transition-metal M content for M = Co. Obviously, the nature of the transition-metal

M strongly influenced the catalytic activity of the CuCeMgAlO system. Indeed, in terms of both T_{50} and T_{90} , the catalytic activity followed the order: CuCeMgAlO < Fe(3)CuCeMgAlO < Mn(3)CuCeMgAlO < Ni(3)CuCeMgAlO < Co(3)CuCeMgAlO. The catalytic behavior of the CuCeMgAlO system was attributed to both the excellent dispersion of copper and the synergy effect between Cu and Ce [21]. According to the XRD analysis, the copper dispersion in the M(3)CuCeMgAlO mixed oxides seemed to be lower compared to CuCeMgAlO, as the segregation of CuO tenorite phase was evidenced. Therefore, to explain their increased activity, an enhanced synergy effect between Cu and Ce in the presence of transition-metal cations M should be taken into consideration, as suggested by the XPS analysis (Figure S4) and in line with previously reported results [22–26]. Indeed, the synergistic interaction between M, Cu, and Ce seemed to be a more important factor affecting the catalytic performance than the degree of crystallinity and surface area of the M(3)CuCeMgAlO materials, in agreement with previously reported results [25]. It is noteworthy that the order of activity observed did not follow the easiness of reduction for the M(3)CuCeMgAlO mixed oxides, suggesting that the most reducible species in the H_2 -TPR experiments were not necessarily the most active in the reaction conditions. On the other hand, the lowest activity of the Fe(3)CuCeMgAlO catalyst in the M(3)CuCeMgAlO series could be correlated to the partial reduction of Cu observed in H_2 -TPR experiments. Keeping this in mind, the superior activity of the Fe(3)CuCeMgAlO compared to the unpromoted CuCeMgAlO system, mainly in terms of intrinsic reaction rate, can only be explained by a synergistic interaction between Fe, Cu, and Ce.

For the most active Co(3)CuCeMgAlO catalyst the T_{50} value was 25 °C lower than that of the M-free CuCeMgAlO catalyst and only 19 °C higher than that of the reference Pd/Al₂O₃ catalyst. Moreover, the complete conversion of methane was achieved over the Co(3)CuCeMgAlO system at a temperature close to that corresponding to the Pd/Al₂O₃ catalyst ($T_{100} \approx 570$ °C). Notably, both specific and intrinsic activities of the Co(3)CuCeMgAlO catalyst calculated at 400 °C (Table 7) showed the superiority of this system, and, hence, the effect of Co content on its catalytic performance was studied. It appeared that the cobalt content strongly influenced, in a complex manner, the catalytic activity of the Co(x)CuCeMgAlO catalysts (Figure 10b), which, in terms of both T_{50} and T_{90} and specific and intrinsic rates, followed the order: CuCeMgAlO < Co(1)CuCeMgAlO < Co(9)CuCeMgAlO < Co(6)CuCeMgAlO < Co(3)CuCeMgAlO. In other words, the catalytic activity passed through a maximum, corresponding to the Co(3)CuCeMgAlO system with increasing the Co content from 1 to 9 at.%. This evolution could be explained taking into consideration an interplay between the Cu-Co-Ce synergistic interaction and the segregation of CuO tenorite phase, the latter going increasingly with increasing the Co content, as evidenced by the X-ray diffraction (Figure 2b) and SEM analyses (Figure S3). Indeed, for Co contents lower than 3 at.%, the amount of promoter involved in the synergistic interaction with Cu and Ce was too low, the copper itself being partially not accessible, as shown in the H_2 -TPR experiments, and, hence, the density of the most active Cu-Co-Ce catalytic sites was lower. For Co contents higher than 3 at.%, the strong segregation of CuO phase took place, resulting again in a decrease of the amount of the most active Cu-Co-Ce catalytic sites compared to the Co(3)CuCeMgAlO system, which was the most active catalyst in this series. Moreover, it was observed that both the rate of methane transformation and the Co^{3+}/Co^{2+} surface atomic ratio roughly followed the same trend when plotted as a function of the Co content x in the Co(x)CuCeMgAlO catalysts (Figure 11). This suggests that the Co^{3+}/Co^{2+} surface atomic ratio is another factor determining the activity of these catalysts in methane combustion, in agreement with the literature [8].

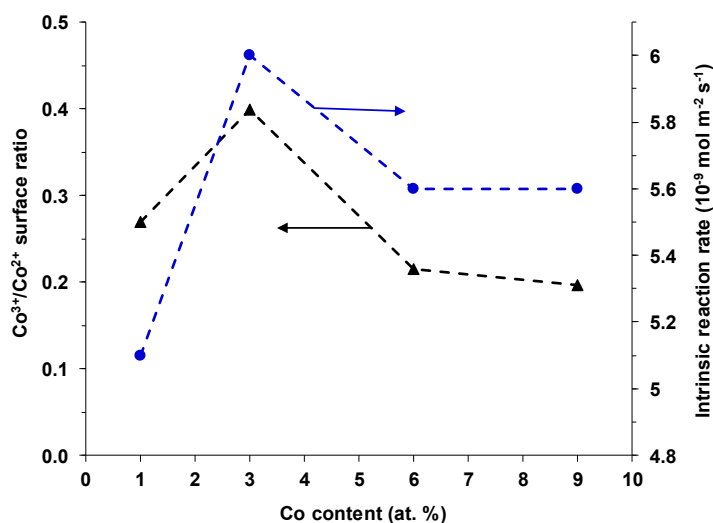


Figure 11. Intrinsic rate of methane conversion measured at 400 °C and $\text{Co}^{3+}/\text{Co}^{2+}$ surface atomic ratio as a function of the Co content in the $\text{Co}(x)\text{CuCeMgAlO}$ catalysts.

Interestingly, pretty good linear correlations were observed between both Cu^{2+}/Cu and Ce^{4+}/Ce surface atomic ratios and the rate of methane transformation over $\text{Co}(x)\text{CuCeMgAlO}$ catalysts (Figure 12), clearly suggesting that Cu^{2+} and Ce^{4+} surface species were also involved in the catalytic process. Notably, all these correlations showing the increase of the reaction rate with increasing Co^{3+} , Cu^{2+} , and Ce^{4+} surface concentrations unambiguously demonstrated that the synergistic interaction between these species was a key factor controlling the activity of the $\text{Co}(x)\text{CuCeMgAlO}$ catalysts in the complete oxidation of methane. The absence of these correlations for the $\text{M}(3)\text{CuCeMgAlO}$ series does not necessarily minimize the role of the M-Cu-Ce synergistic interaction, but rather shows that the nature of the cation M influenced the physicochemical characteristics and, hence, the catalytic properties of these materials in a complex manner. Thus, for example, while the surface concentration of Fe is by ca. 30% lower compared with its bulk concentration, the surface concentrations of Mn, Co, and Ni are by ca. 73, 74, and 178%, respectively, higher. Also, for $\text{Co}(3)$ - and $\text{Ni}(3)\text{CuCeMgAlO}$, the surface of the catalysts is enriched in Cu compared to the bulk composition, while for $\text{Mn}(3)$ - and $\text{Fe}(3)\text{CuCeMgAlO}$ it is poorer. Moreover, for $\text{Fe}(3)$ -, $\text{Co}(3)$ -, and $\text{Ni}(3)\text{CuCeMgAlO}$, the Cu/Ce surface atomic ratio is significantly higher than the bulk ratio, while for $\text{Mn}(3)\text{CuCeMgAlO}$ it is lower. All these differences, which were not observed in the $\text{Co}(x)\text{CuCeMgAlO}$ series, could have been at the origin of the different behavior of the $\text{M}(3)\text{CuCeMgAlO}$ series.

No correlation could be observed between the catalytic performance and the reducibility of the mixed oxide in the $\text{M}(3)\text{CuCeMgAlO}$ series. However, for the $\text{Co}(x)\text{CuCeMgAlO}$ series, a good linear correlation between the rate of methane conversion and the hydrogen consumption in the H_2 -TPR experiments was noticed (Figure 13). On one hand, this suggested that all the reducible species evidenced in the H_2 -TPR experiments were involved in the catalytic oxidation of methane over the Co-promoted CuCeMgAlO catalysts, in line with a Cu-Co-Ce synergistic interaction, and, on the other hand, confirmed the heterogeneous redox mechanism for methane combustion over these catalytic materials. Notably, the correlation reaction rate – reducibility was previously reported for several mixed oxides catalysts obtained from LDH precursors containing Cu [12,14,50] and Ce [33] for the complete oxidation of methane.

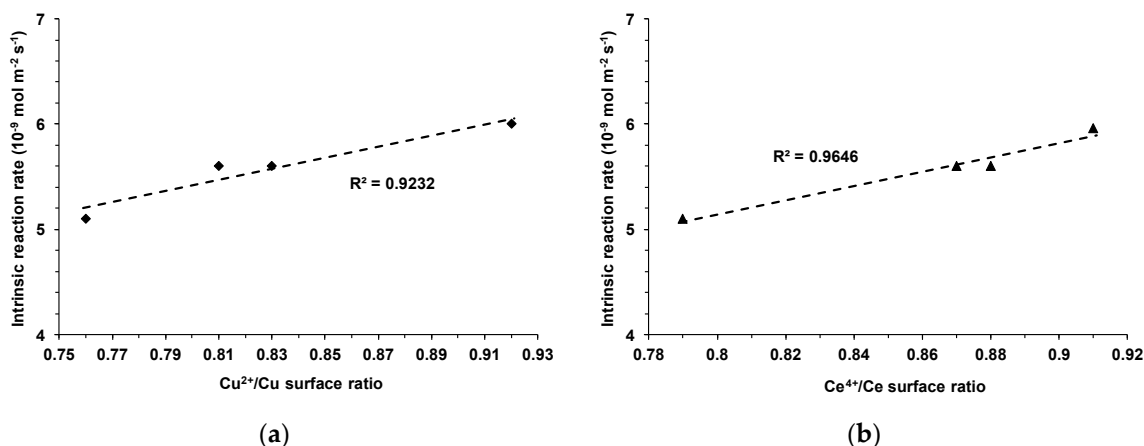


Figure 12. Intrinsic rate of methane conversion measured at 400 °C as a function of (a) Cu^{2+}/Cu and (b) Ce^{4+}/Ce surface atomic ratios in the $\text{Co}(x)\text{CuCeMgAlO}$ catalysts.

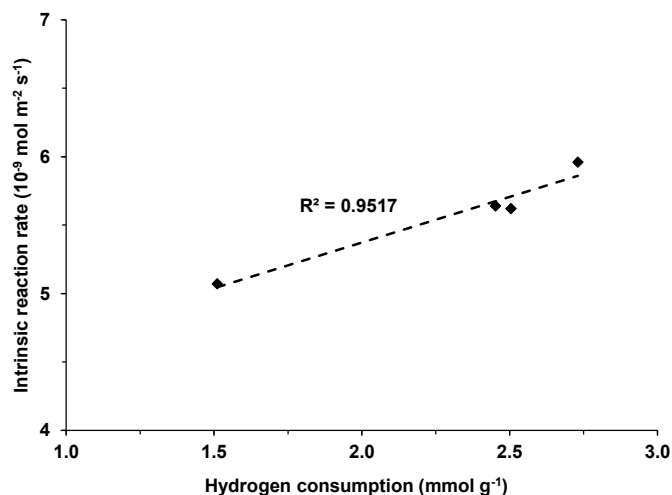


Figure 13. Intrinsic rate of methane conversion measured at 400 °C vs. hydrogen consumption in the H_2 -TPR experiments for the $\text{Co}(x)\text{CuCeMgAlO}$ catalysts.

The apparent activation energies (E_a) for the transformation of methane on the transition metal-promoted CuCeMgAlO catalysts were calculated from the slope of the low-conversion linear part of the $\ln r$ vs. $10^3/T$ Arrhenius plots (Figure S10) and are presented in Table 7. It can be observed that the activation energy values for the $\text{M}(3)\text{CuCeMgAlO}$ catalysts were slightly higher than that corresponding to M -free CuCeMgAlO . This difference can be attributed to the segregation of CuO in the former. However, their enhanced catalytic activity was obviously due to a greater density of highly active sites consisting of CuO synergistically interacting with both M and Ce cations, the different nature of the cation M accounting for the differences observed in the activation energies of the $\text{M}(3)\text{CuCeMgAlO}$ series. Although the lowest activation energy in this series corresponded to the most active $\text{Co}(3)\text{CuCeMgAlO}$ catalyst, it did not parallel the catalytic activity likely due to different densities of surface active sites. Regarding the activation energy for the $\text{Co}(x)\text{CuCeMgAlO}$ series, it was slightly lower for $\text{Co}(1)\text{CuCeMgAlO}$ system compared to CuCeMgAlO , in line with their relative activities, while it was higher for the other Co -containing systems and varied within a narrow range irrespective of the Co content. Also, it did not parallel the catalytic activity, as different densities of active sites may exist on the surface of $\text{Co}(x)\text{CuCeMgAlO}$ mixed oxides.

Although similar LDH-derived Cu- and/or Ce-containing mixed oxides [12,21,33,50] catalysts were shown to display good stabilities during the total oxidation of methane, the stability on stream of the most active Co(3)CuCeMgAlO catalyst was tested at 520 °C for 60 h. No change of the catalytic performance could be observed (Figure S11), suggesting that Co(3)CuCeMgAlO system is stable on stream, at least for the reaction conditions and the reaction time chosen.

3. Materials and Methods

3.1. Catalysts Preparation

Two series of multicationic LDH-derived mixed oxides were prepared by thermal decomposition of their corresponding LDH precursors obtained by coprecipitation under ambient atmosphere. The first series consisted of four M(3)CuCeMgAlO mixed oxides containing 3 at.% M (M = Mn, Fe, Co, Ni), 15 at.% Cu, 10 at.% Ce (at.% with respect to cations), and with Mg/Al atomic ratio of 3. The second series consisted of four Co(x)CuCeMgAlO mixed oxides with x = 1, 3, 6, and 9 at.%, while keeping constant the Cu and Ce contents and the Mg/Al atomic ratio.

In a typical procedure, 200 mL of a mixed metal salts solution containing the appropriate amounts of metal nitrates and a solution of NaOH (2 M) were simultaneously added dropwise with controlled rate (to maintain the pH close to 10) into a beaker containing 200 mL of cerium nitrate solution at room temperature. After the precipitation, the slurry was aged under vigorous stirring at 80 °C overnight and, after cooling at room temperature, the suspension was separated by centrifugation. The precipitate was washed with deionized water and then dried overnight at 80 °C to obtain the LDH precursors. The latter were finally calcined in air at 750 °C for 8 h in a muffle furnace, with a heating rate of 2 °C min⁻¹, leading to the mixed oxide catalysts. The CuCeMgAlO mixed oxide was obtained following the same protocol. The following chemicals were used for the preparation of the catalysts: Mg(NO₃)₂·6H₂O (Sigma-Aldrich), Al(NO₃)₃·9H₂O (Fluka), Cu(NO₃)₂·3H₂O (Sigma-Aldrich), Ce(NO₃)₃·6H₂O (Aldrich), Mn(NO₃)₂·4H₂O (Sigma-Aldrich), Fe(NO₃)₃·9H₂O (Aldrich), Co(NO₃)₂·6H₂O (Aldrich), Ni(NO₃)₂·6H₂O (Sigma-Aldrich), and NaOH (Fluka).

3.2. Catalysts Characterization

Powder X-ray diffraction (XRD) patterns of both precursors and mixed oxides were recorded on a Bruker-AXS D8 Advance diffractometer (Bruker Corporation, Billerica, MA, USA) equipped with a LynxEye 1D detector, a Cu-K α ($\lambda = 0.15406$ nm) radiation source, and a scintillation counter detector. They were recorded over the 5–70° 2 θ angular range with a 0.02° step size and using a counting time of 1 s per point. Crystalline phases were identified using standard powder diffraction files (PDF).

The thermogravimetric and differential thermal analyses (TG-DTG-DTA) of the LDH precursors were carried out using a Labsys 1200 SETARAM instrument, in the following conditions: linear heating rate of 10 °C min⁻¹ from room temperature to 900 °C, dynamic synthetic air atmosphere (flow rate 16.66 mL min⁻¹), Al₂O₃ crucible, and sample weight of approximately 20 mg.

Transmission electron microscopy (TEM) images were obtained on a TopCon 2100 FCs microscope with an accelerating voltage of 200 kV. The samples were dispersed in ethanol in an ultrasonic bath for several minutes, and then deposited on a Cu grid and dried at room temperature.

Scanning electron microscopy (SEM) together with X-ray energy dispersion analysis (EDX) were used to monitor the morphology and chemical composition of both precursors and mixed oxides. SEM/EDX examination was performed using a Gemini 500 microscope from Zeiss International GmbH, equipped with a Quantax XFlash 6/10 energy dispersive spectrometry detector from Bruker (Billerica, MA, USA) for elemental analysis. The images for all samples were taken at 5.000 X magnification and 5 kV acceleration

voltage using the secondary electrons (SE) detector. For EDX analysis, an acceleration voltage of 15 kV was employed. Four different points were analyzed on each sample.

X-ray photoelectron spectroscopy (XPS) was employed to determine the chemical state of the elements on the surface of the mixed oxide catalysts with a SPECS spectrometer equipped with a PHOIBOS 150 analyzer using a monochromatic Al K α radiation source (1486.7 eV). The acquisition was operated at a pass energy of 20 eV for the individual spectral lines and 50 eV for the extended spectra. The analysis of the spectra was performed with the Spectral Data Processor v2.3 software using Voigt functions and usual sensitivity factors.

Diffuse reflectance electronic spectra were recorded in the range 200–1500 nm, using Spectralon as a standard, with a Jasco V 670 spectrophotometer. The obtained reflectance spectra were converted into the dependencies of Kubelka–Munk function on the absorption energy.

The textural characterization was performed using the conventional nitrogen adsorption/desorption method, with a Micromeritics ASAP 2010 automatic equipment. The surface areas were calculated using the Brunauer–Emmett–Teller (BET) method in the relative pressure, P/P_0 , region 0.065–0.2, while the pore sizes were determined by the Barrett–Joyner–Halenda (BJH) method from the nitrogen desorption branch. Prior to nitrogen adsorption, the oxide samples were degassed at 300 °C for 12 h.

The reducibility of the catalysts was studied by temperature-programmed reduction under hydrogen (H_2 -TPR). Experiments were performed using a Porotec TPDRO 1100 device (Thermo Fischer Scientific Inc., Waltham, MA, USA) equipped with a thermal conductivity detector (TCD). Prior to the analysis, the samples (ca. 0.05 g) were treated at 200 °C for 1 h in He flow (20 mL min⁻¹) to ensure the surface cleaning, then they were cooled to room temperature under helium flow. The analysis was performed by heating the samples under a 5% H_2 /Ar gas flow (20 mL min⁻¹) at a constant rate of 10 °C min⁻¹ from room temperature up to 800 °C.

3.3. Catalytic Test

The catalytic total oxidation of methane over the transition metal-promoted CuCeMgAlO mixed oxide catalysts was carried out in a fixed bed quartz tube down-flow reactor at atmospheric pressure. If not otherwise specified, a mixture of CH_4 and air containing 1 vol.% methane was passed through 1 cm³ (ca. 0.9 g) catalyst bed with a total flow rate of 267 mL min⁻¹ corresponding to a gas hourly space velocity (GHSV) of 16,000 h⁻¹. For comparison, an industrially used Pd/Al₂O₃ catalyst (supplied by ARPECHIM Pitești, Romania) was tested in methane combustion in similar conditions. Before testing, the catalyst was pretreated for 30 min in a stream of nitrogen at 600 °C for cleaning its surface. After pretreatment, the catalyst was cooled down to 300 °C and the reaction was started by introducing the reaction mixture. Activity measurements were performed by increasing the reaction temperature from 300 to 650 °C at regular intervals. The reactants and product gases were analyzed on-line by a Clarus 500 Gas-Chromatograph equipped with a thermal conductivity detector, using two packed columns in series (6 ft Hayesep and 10 ft molecular sieve 5 Å). The catalysts activity was characterized by T_{10} , T_{50} , and T_{90} , representing the temperatures of methane conversions of 10, 50, and 90%, respectively. The conversion was calculated as the amount of methane transformed in the reaction divided by the amount that was fed to the reactor. Complete selectivity to CO₂ and H₂O was always observed. The carbon balance was satisfactory in all runs to within $\pm 2\%$.

4. Conclusions

Two series of transition metal-promoted CuCeMgAlO mixed oxides, namely M(3)CuCeMgAlO (3 at.% M = Mn, Fe, Co and Ni) and Co(x)CuCeMgAlO ($x = 1, 3, 6$ and 9 at.% Co), with fixed Cu and Ce contents of 15 and 10 at.%, respectively, and Mg/Al mol ratio of 3, were prepared by thermal decomposition

at 750 °C of precursors consisting of well-crystallized LDH phase together with poorly crystallized boehmite AlOOH side phase. They were mesoporous materials with surface areas lower than that of the parent CuCeMgAlO mixed oxide, in the range from 66 to 78 m² g⁻¹, and consisted of periclase-like Mg(Al)O mixed oxide, CeO₂ fluorite, and CuO tenorite phases. The segregation of the CuO tenorite phase increased with the Co content in the Co(x)CuCeMgAlO series. The nature of the transition-metal M for the M(3)CuCeMgAlO catalysts series and the Co content for the Co(x)CuCeMgAlO series strongly influenced, in a complex manner, their physicochemical characteristics and, hence, their catalytic performance in the complete oxidation of methane. No clear correlations could be observed between the catalytic performance and the physicochemical characteristics of the mixed oxide in the M(3)CuCeMgAlO series. However, their enhanced activity compared to the M-free CuCeMgAlO system was attributed to an enhanced synergistic interaction between Cu and Ce in the presence of transition-metal cations M. On the other hand, the catalytic activity in the Co(x)CuCeMgAlO series was shown to increase with increasing of both the Co³⁺, Cu²⁺, and Ce⁴⁺ surface concentrations and the catalyst reducibility, unambiguously demonstrating that the synergistic interaction between these species was a key factor controlling their catalytic behavior in the complete oxidation of methane. The Co-promoted CuCeMgAlO mixed oxide with 3 at.% Co was shown to be the most active catalyst in both series, with a T₅₀ value of only ca. 20 °C higher than that of a reference Pd/Al₂O₃ catalyst. Its enhanced catalytic activity was attributed to an excellent Cu-Co-Ce synergistic interaction. A good stability on stream of the Co(3)CuCeMgAlO catalyst was also noticed.

Supplementary Materials: The following are available online at <http://www.mdpi.com/2073-4344/10/6/613/s1>, Figure S1: TG-DTG-DTA curves of selected LDH precursors. Figure S2: TEM images of Mn(3)-, Ni(3)-, Co(3)-, and Co(9)CuCeMgAlO mixed oxides. Figure S3: SEM images of the LDH-derived M(3)CuCeMgAlO and Co(x)CuCeMgAlO mixed oxides. Figure S4: Ce⁴⁺/Ce vs. Cu²⁺/Cu surface ratios for (a) M(3)CuCeMgAlO and (b) Co(x)CuCeMgAlO mixed oxide series. Figure S5: Al 2p core level XPS spectra of the M-free CuCeMgAlO, M(3)CuCeMgAlO, and Co(x)CuCeMgAlO mixed oxides. Figure S6: Mg 2p core level XPS spectra and the corresponding Auger Mg KLL spectra of the CuCeMgAlO, M(3)CuCeMgAlO, and Co(x)CuCeMgAlO mixed oxides. Figure S7: The X-ray photoelectron profiles of Mn 2p, Fe 2p, and Ni 2p of the Mn(3)-, Fe(3)-, and Ni(3)CuCeMgAlO mixed oxides, respectively. Figure S8: Nitrogen adsorption/desorption isotherms at -196 °C of (a) CuCeMgAlO and M(3)CuCeMgAlO and (b) Co(x)CuCeMgAlO mixed oxides. Figure S9: Pore size distributions of the CuCeMgAlO, M(3)CuCeMgAlO, and Co(x)CuCeMgAlO mixed oxides. Figure S10: Arrhenius plots for the combustion of methane over CuCeMgAlO, M(3)CuCeMgAlO, and Co(x)CuCeMgAlO catalysts. Figure S11: Effect of the time on stream on the catalytic performance of Co(3)CuCeMgAlO mixed oxide at 520 °C. Table S1: Surface composition of the mixed oxide catalysts determined by XPS analysis. Table S2: XPS and Auger data for Al and Mg in the CuCeMgAlO, M(3)CuCeMgAlO, and Co(x)CuCeMgAlO mixed oxides.

Author Contributions: Conceptualization, I.-C.M.; methodology, I.P. and M.F.; validation, I.P., M.F., and C.N.; investigation, H.M.S.A.-A., M.M.T., I.F., L.N.L., M.B., and C.N.; resources, I.-C.M. and M.F.; data curation, I.P., M.B., M.M.T., and C.N.; writing—original draft preparation, H.M.S.A.-A. and I.-C.M.; writing—review and editing, I.-C.M. and M.F.; visualization, H.M.S.A.-A., I.F., C.N., and I.-C.M.; supervision, I.-C.M. and M.F.; project administration, I.-C.M. All authors have read and agreed to the published version of the manuscript.

Funding: This research received no external funding.

Conflicts of Interest: The authors declare no conflict of interest.

References

1. Kuśtrowski, P.; Rokicińska, A.; Kondratowicz, T. Abatement of volatile organic compounds emission as a target for various human activities including energy production. *Adv. Inorg. Chem.* **2018**, *72*, 385–419. [[CrossRef](#)]
2. Heck, R.M.; Farrauto, R.J.; Gulati, S.T. *Catalytic Air Pollution Control: Commercial Technology*, 3rd ed.; John Wiley & Sons, Inc.: Hoboken, NJ, USA, 2009.
3. Morales, M.R.; Barbero, B.P.; Cadús, L.E. Total oxidation of ethanol and propane over Mn-Cu mixed oxide catalysts. *Appl. Catal. B Environ.* **2006**, *67*, 229–236. [[CrossRef](#)]

4. Craciun, R.; Nentwick, B.; Hadjiivanov, K.; Knözinger, H. Structure and redox properties of $\text{MnO}_x/\text{Yttrium-stabilized zirconia (YSZ)}$ catalyst and its used in CO and CH_4 oxidation. *Appl. Catal. A Gen.* **2003**, *243*, 67–79. [[CrossRef](#)]
5. Shahzad Kamal, M.; Razzak, S.A.; Hossain, M.M. Catalytic oxidation of volatile organic compounds (VOCs)-A review. *Atmos. Environ.* **2016**, *140*, 117–134. [[CrossRef](#)]
6. Tomatis, M.; Xu, H.H.; He, J.; Zhang, X.D. Recent development of catalysts for removal of volatile organic compounds in flue gas by combustion: A review. *J. Chem.* **2016**, *2016*, 8324826. [[CrossRef](#)]
7. Marcu, I.C.; Urdă, A.; Popescu, I.; Hulea, V. Layered double hydroxides-based materials as oxidation catalysts. In *Sustainable Nanosystems Development, Properties, and Applications*; Putz, M.V., Mirica, M.C., Eds.; IGI Global: Hershey, PA, USA, 2017; Chapter 3; pp. 59–121. [[CrossRef](#)]
8. Urdă, A.; Popescu, I.; Marcu, I.C. Nanocrystalline spinel catalysts for volatile organic compounds abatement. In *Nanostructured Catalysts for Environmental Applications*; Piumetti, M., Bensaid, S., Eds.; Springer: Heidelberg, Germany, 2020; accepted.
9. Cavani, F.; Trifirò, F.; Vaccari, A. Hydrotalcite-type anionic clays: Preparation, properties and applications. *Catal. Today* **1991**, *11*, 173–301. [[CrossRef](#)]
10. Lopez, M.; Sherwood, O.A.; Dlugokencky, E.J.; Kessler, R.; Giroux, L.; Worthy, D.E.J. Isotopic signatures of anthropogenic CH_4 sources in Alberta, Canada. *Atmos. Environ.* **2017**, *164*, 280–288. [[CrossRef](#)]
11. Tanasoi, S.; Mitran, G.; Tanchoux, N.; Cacciaguerra, T.; Fajula, F.; Săndulescu, I.; Tichit, D.; Marcu, I.C. Transition metal-containing mixed oxides catalysts derived from LDH precursors for short-chain hydrocarbons oxidation. *Appl. Catal. A Gen.* **2011**, *395*, 78–86. [[CrossRef](#)]
12. Tanasoi, S.; Tanchoux, N.; Urdă, A.; Tichit, D.; Săndulescu, I.; Fajula, F.; Marcu, I.C. New Cu-based mixed oxides obtained from LDH precursors, catalysts for methane total oxidation. *Appl. Catal. A Gen.* **2009**, *363*, 135–142. [[CrossRef](#)]
13. Jiang, Z.; Hao, Z.; Yu, J.; Hou, H.; Hu, C.; Su, J. Catalytic combustion of methane on novel catalysts derived from Cu–Mg/Al-hydrotalcites. *Catal. Lett.* **2005**, *99*, 157–163. [[CrossRef](#)]
14. Răciulete, M.; Layrac, G.; Tichit, D.; Marcu, I.C. Comparison of Cu_xZnAlO mixed oxide catalysts derived from multicationic and hybrid LDH precursors for methane total oxidation. *Appl. Catal. A Gen.* **2014**, *477*, 195–204. [[CrossRef](#)]
15. Răciulete, M.; Layrac, G.; Papa, F.; Negrilă, C.; Tichit, D.; Marcu, I.C. Influence of Mn content on the catalytic properties of Cu-(Mn)-Zn-Mg-Al mixed oxides derived from LDH precursors in the total oxidation of methane. *Catal. Today* **2018**, *306*, 276–286. [[CrossRef](#)]
16. Kovanda, F.; Jirátová, R.; Rymes, J.; Kolousek, D. Characterization of activated Cu/Mg/Al hydrotalcites and their catalytic activity in toluene combustion. *Appl. Clay Sci.* **2001**, *18*, 71–80. [[CrossRef](#)]
17. Palacio, L.A.; Velásquez, J.; Echavarría, A.; Faro, A.; Ribeiro, F.R.; Ribeiro, M.F. Total oxidation of toluene over calcined trimetallic hydrotalcites type catalysts. *J. Hazard. Mater.* **2010**, *177*, 407–413. [[CrossRef](#)] [[PubMed](#)]
18. Chmielarz, L.; Piwowarska, Z.; Rutkowska, M.; Wojciechowska, M.; Dudek, B.; Witkowski, S.; Michalik, M. Total oxidation of selected mono-carbon VOCs over hydrotalcite originated metal oxide catalysts. *Catal. Commun.* **2012**, *17*, 118–125. [[CrossRef](#)]
19. Kovanda, F.; Jirátová, K. Supported layered double hydroxide-related mixed oxides and their application in the total oxidation of volatile organic compounds. *Appl. Clay Sci.* **2011**, *53*, 305–316. [[CrossRef](#)]
20. Jiang, Z.; Kong, L.; Chu, Z.; France, L.J.; Xiao, T.; Edwards, P.P. Catalytic combustion of propane over mixed oxides derived from $\text{Cu}_x\text{Mg}_{3-x}\text{Al}$ hydrotalcites. *Fuel* **2012**, *96*, 257–263. [[CrossRef](#)]
21. Al-Aani, H.M.S.; Iro, E.; Chirra, P.; Fechete, I.; Badea, M.; Negrilă, C.; Popescu, I.; Olea, M.; Marcu, I.C. $\text{Cu}_x\text{CeMgAlO}$ mixed oxide catalysts derived from multicationic LDH precursors for methane total oxidation. *Appl. Catal. A Gen.* **2019**, *586*, 117215. [[CrossRef](#)]
22. Zhu, H.; Chen, Y.; Gao, Y.; Liu, W.; Wang, Z.; Cui, C.; Liu, W.; Wang, L. Catalytic oxidation of CO on mesoporous codoped ceria catalysts: Insights into correlation of physicochemical property and catalytic activity. *J. Rare Earths* **2019**, *37*, 961–969. [[CrossRef](#)]

23. Kim, H.J.; Lee, G.; Jang, M.G.; Noh, K.J.; Han, J.W. Rational design of transition metal co-doped ceria catalysts for low-temperature CO oxidation. *ChemCatChem* **2019**, *11*, 2288–2296. [[CrossRef](#)]
24. Guo, X.; Qiu, Z.; Mao, J.; Zhou, R. Doping effect of transition metals (Zr, Mn, Ti and Ni) on well shaped CuO/CeO₂(rod): Nano/micro structure and catalytic performance for selective oxidation of CO in excess H₂. *Phys. Chem. Chem. Phys.* **2018**, *20*, 25983–25994. [[CrossRef](#)] [[PubMed](#)]
25. Park, Y.; Kim, S.K.; Pradhan, D.; Sohn, Y. Surface treatment effects on CO oxidation reactions over Co, Cu, and Ni-doped and codoped CeO₂ catalysts. *Chem. Eng. J.* **2014**, *250*, 25–34. [[CrossRef](#)]
26. Górecka, S.; Pacultová, K.; Górecki, K.; Smýkalová, A.; Pamin, K.; Obalová, L. Cu-Mg-Fe-O-(Ce) complex oxides as catalysts of selective catalytic oxidation of ammonia to dinitrogen (NH₃-SCO). *Catalysts* **2020**, *10*, 153. [[CrossRef](#)]
27. Carja, G.; Dranca, S.; Ciobanu, G.; Husanu, E.; Balasanian, I. Fabrication of mesoporous mixed oxides containing copper and cerium by using substituted anionic clays as precursors. *Mater. Sci. Poland* **2009**, *27*, 909–917.
28. Rives, V.; Ulibarri, M.A. Layered double hydroxides (LDH) intercalated with metal coordination compounds and oxometalates. *Coord. Chem. Rev.* **1999**, *181*, 61–120. [[CrossRef](#)]
29. Tichit, D.; Das, N.; Coq, B.; Durand, R. Preparation of Zr-containing layered double hydroxides and characterization of the acido-basic properties of their mixed oxides. *Chem. Mater.* **2002**, *14*, 1530–1538. [[CrossRef](#)]
30. Balassone, G.; Petti, C.; Mondillo, N.; Taras, L.; Panikorovskii, T.L.; Gennaro, R.; Cappelletti, P.; Altomare, A.; Corriero, N.; Cangiano, M.; et al. Copper minerals at Vesuvius volcano (southern Italy): A mineralogical review. *Minerals* **2019**, *9*, 730. [[CrossRef](#)]
31. Zhang, H.; Zhang, G.; Bi, X.; Chen, X. Facile assembly of a hierarchical core@shell Fe₃O₄@CuMgAl-LDH (layered double hydroxide) magnetic nanocatalyst for the hydroxylation of phenol. *J. Mater. Chem. A* **2013**, *1*, 5934–5942. [[CrossRef](#)]
32. Savova, B.; Filkova, D.; Crişan, D.; Crişan, M.; Răileanu, M.; Drăgan, N.; Galtayries, A.; Védrine, J.C. Neodymium doped alkaline-earth oxide catalysts for propane oxidative dehydrogenation. Part, I. Catalyst characterisation. *Appl. Catal. A Gen.* **2009**, *359*, 47–54. [[CrossRef](#)]
33. Urdă, A.; Popescu, I.; Cacciaguerra, T.; Tanchoux, N.; Tichit, D.; Marcu, I.C. Total oxidation of methane over rare earth cation-containing mixed oxides derived from LDH precursors. *Appl. Catal. A Gen.* **2013**, *464*, 20–27. [[CrossRef](#)]
34. Schofield, P.F.; Henderson, C.M.B.; Redfern, S.A.T.; Van der Laan, G. Cu 2p absorption spectroscopy as a probe for the site occupancy of (Zn_xCu_{1-x})WO₄ solid solution. *Phys. Chem. Miner.* **1993**, *20*, 375–381. [[CrossRef](#)]
35. Biesinger, M.C.; Lau, L.W.M.; Gerson, A.R.; Smart, R.S.C. Resolving surface chemical states in XPS analysis of first row transition metals, oxides and hydroxides: Sc, Ti, V, Cu and Zn. *Appl. Surf. Sci.* **2010**, *257*, 887–898. [[CrossRef](#)]
36. Burroughs, P.; Hamnett, A.; Orchard, A.F.; Thornton, G. Satellite structure in the X-ray photoelectron spectra of some binary and mixed oxides of lanthanum and cerium. *J. Chem. Soc. Dalton Trans.* **1976**, 1686–1698. [[CrossRef](#)]
37. Bêche, E.; Charvin, P.; Perarnau, D.; Abanades, S.; Flamant, G. Ce 3d XPS investigation of cerium oxides and mixed cerium oxide (Ce_xTi_yO_z). *Surf. Interface Anal.* **2008**, *40*, 264–267. [[CrossRef](#)]
38. Yu, X.; Li, G. XPS study of cerium conversion coating on the anodized 2024 aluminum alloy. *J. Alloy Compd.* **2004**, *364*, 193–198. [[CrossRef](#)]
39. *NIST X-ray Photoelectron Spectroscopy Database, NIST Standard Reference Database Number 20*; National Institute of Standards and Technology: Gaithersburg, MD, USA, 2000; p. 20899. [[CrossRef](#)]
40. Cai, T.; Huang, H.; Deng, W.; Dai, Q.; Liu, W.; Wang, X. Catalytic combustion of 1,2-dichlorobenzene at low temperature over Mn-modified Co₃O₄ catalysts. *Appl. Catal. B Environ.* **2015**, *166*, 393–405. [[CrossRef](#)]
41. Grosvenor, A.P.; Biesinger, M.C.; Smart, R.S.C.; McIntyre, N.S. New interpretations of XPS spectra of nickel metal and oxides. *Surf. Sci.* **2006**, *600*, 1771–1779. [[CrossRef](#)]
42. Emamdoust, A.; La Parola, V.; Pantaleo, G.; Testa, M.L.; Farjami Shayesteh, S.; Venezia, A.M. Partial oxidation of methane over SiO₂ supported Ni and NiCe catalysts. *J. Energy Chem.* **2020**, *47*, 1–9. [[CrossRef](#)]

43. Biesinger, M.C.; Payne, B.P.; Grosvenor, A.P.; Lau, L.W.M.; Gerson, A.R.; Smart, R.S.C. Resolving surface chemical states in XPS analysis of first row transition metals, oxides and hydroxides: Cr, Mn, Fe, Co and Ni. *Appl. Surf. Sci.* **2011**, *257*, 2717–2730. [[CrossRef](#)]
44. Chen, J.; Lin, J.; Chen, J.; Wang, J. Effect of small molecular organic acids on the structure and catalytic performance of sol–gel prepared cobalt cerium oxides towards toluene combustion. *Catalysts* **2019**, *9*, 483. [[CrossRef](#)]
45. Lever, A.B.P. *Inorganic Electronic Spectroscopy*, 2nd ed.; Elsevier: Amsterdam, The Netherlands; London, UK; New York, NY, USA, 1984; pp. 553–572.
46. Basag, S.; Kocoł, K.; Piwowarska, Z.; Rutkowska, M.; Baran, R.; Chmielarz, L. Activating effect of cerium in hydrotalcite derived Cu-Mg-Al catalysts for selective ammonia oxidation and the selective reduction of NO with ammonia. *Reac. Kinet. Mech. Catal.* **2017**, *121*, 225–240. [[CrossRef](#)]
47. Thommes, M.; Kaneko, K.; Neimark, A.V.; Olivier, J.P.; Rodriguez-Reinoso, F.; Rouquerol, J.; Sing, K.S.W. Physisorption of gases, with special reference to the evaluation of surface area and pore size distribution (IUPAC Technical Report). *Pure Appl. Chem.* **2015**, *87*, 1051–1069. [[CrossRef](#)]
48. Beckers, J.; Rothenberg, G. Redox properties of doped and supported copper-ceria catalysts. *Dalton Trans.* **2008**, 6573–6578. [[CrossRef](#)]
49. Zhao, H.; Fang, K.; Zhou, J.; Lin, M.; Sun, Y. Direct synthesis of methyl formate from syngas on Cu-Mn mixed oxide catalyst. *Int. J. Hydrogen Energy* **2016**, *41*, 8819–8828. [[CrossRef](#)]
50. Popescu, I.; Tanchoux, N.; Tichit, D.; Marcu, I.C. Total oxidation of methane over supported CuO: Influence of the Mg_xAl_yO support. *Appl. Catal. A Gen.* **2017**, *538*, 81–90. [[CrossRef](#)]



© 2020 by the authors. Licensee MDPI, Basel, Switzerland. This article is an open access article distributed under the terms and conditions of the Creative Commons Attribution (CC BY) license (<http://creativecommons.org/licenses/by/4.0/>).